ELSEVIER

Journal of Nuclear Materials 289 (2001) 115–121

journal of nuclear materials

www.elsevier.nl/locate/jnucmat

Section 3. Fundamental radiation effects in inert matrix fuels and nuclear waste materials

Behaviour of implanted xenon in yttria-stabilised zirconia as inert matrix of a nuclear fuel

C. Degueldre [a,*], M. Pouchon [a], M. Döbeli [a], K. Sickafus [b], K. Hojou [c], G. Ledergerber [a,1], S. Abolhassani-Dadras [a]

[a] *Paul Scherrer Institut, 5232 Villigen-PSI, Switzerland*
[b] *Los Alamos National Laboratory, MST11, Los Alamos, NM 87545, USA*
[c] *Japanese Atomic Energy Research Institute, Tokai-mura, Ibaraki-ken, 319-11, Japan*

Abstract

A zirconia-based fuel is studied for use of plutonium in light water reactors. Among the relevant properties for a nuclear fuel, efficient retention of fission products is required since the fuel matrix constitutes the first barrier against fission product release. To study the retention of xenon, its stopping power and its diffusion properties within $(Er,Y,Pu,Zr)O_2$ potential inert matrix fuel (IMF) are investigated. Stopping and range of ions in matter (SRIM) calculations were carried out to estimate the average penetration depth of Xe ions as a function of their incident energy and of the material composition. To study its diffusion properties, Xe was implanted into yttria-stabilised zirconia (YSZ) to a depth of around 100 nm from the surface. After successive heat treatments to a maximum temperature of 1773 K, quantitative Xe depth profiles were determined by Rutherford backscattering. No profile modification by diffusion was observed. The behaviour of Xe is investigated at the subnanoscopic level and compared with the results obtained with zirconia samples implanted with Cs or I, as well as with Xe in UO_2.

PACS: 61.80.Jh; 61.82.Ms; 61.85.+p; 66.30.Jt; 81.05.Je

1. Introduction

Stabilised zirconia is studied as potential inert matrix fuel (IMF) component for burning excess plutonium in light water reactors [1]. Stabilised zirconia is foreseen as a full pellet solid solution for example by Degueldre and Paratte [2], Vettraino et al. [3] and Sickafus et al. [4] or as part of a composite material for example as a cercer as suggested by Konings et al. [5] and Yamashita et al. [6], or as a cermet [7]. We focus IMF research on an yttria-stabilised zirconia (YSZ) of composition close to $Er_{0.05}Y_{0.10}Pu_{0.10}Zr_{0.75}O_{1.925}$ as solid solution or on a Zr– or $MgAl_2O_4$–$Er_{0.05}Y_{0.10}Pu_{0.10}Zr_{0.85}O_{1.925}$ composite material. For radioprotection safety reasons, the behaviour of specific fission products such as xenon, iodine and cesium in YSZ is currently studied and the first results were recently reported in specific studies [8–10]. Xenon is, however, also a relevant fission product from the neutronics point of view. Consequently, xenon retention must be assessed in the fuel. Xenon is known as an inert gas fission product that currently diffuses from the fuel pellets towards intergranular spaces, pores or towards the gap between the fuel and cladding [11].

Early in the nineties, YSZ was irradiated by xenon ions, and zirconia was studied for its mechanical property changes by Norton et al. [12] and Levine et al. [13,14]. Fleischer et al. [15], for example, used ion channelling and transmission electron microscopy (TEM) to examine 240 keV Xe ion implanted in YSZ. Hardness increases up to a fluence of 7.5×10^{15} cm^{-2} followed by a decrease (up to 3×10^{16} cm^{-2}) were observed. The author also noted that because noble gases are immiscible with the matrix, they may coalesce to form inclusions. At fluences greater than 3×10^{16} cm^{-2}

* Corresponding author. Fax: +41-56 310 2205.
E-mail address: claude.degueldre@psi.ch (C. Degueldre).
[1] Present address: Leibstadt Nuclear Power Plant, 5325 Leibstadt, Switzerland.

0022-3115/01/$ - see front matter
PII: S0022-3115(00)00690-5

the formation of fluid or solid noble gas inclusion was found in YSZ. The pressure of the solid inclusions has been calculated to be around 1.5 GPa. For shallow implants, the presence of the implanted species can lead to high compressive stresses in the material subsurface. Fractures may be formed that result in copious emission of xenon. Norton et al. [16] studied the microcracking generated by xenon implantation by analysing the SEM micrographs of the surface of cubic zirconia samples.

In Japan, Sasajima et al. [17] studied the effect of 60 keV Xe implantation into monocrystal specimens at several temperatures in the range 300–1473 K for an in situ TEM analysis. Amorphisation did not occur in zirconia irradiated up to the fluence of 1.8×10^{16} cm^{-2} at all irradiation temperatures. These tests, however, apply for 100 nm thick samples irradiated with low energy ions. The swelling of the samples was reported to be 1% and 4% for the highest doses applied at 923 and 1473 K, respectively.

At Los Alamos, Yu et al. [18,19]; Sickafus et al. [20]; Yasuda et al. [21] studied the effect of Xe implantation into monocrystals of YSZ. Full-stabilised zirconia crystals (Y, Ca and Er dopants acting as stabilisers) were irradiated with 340–400 keV Xe^{2+} at temperatures ranging from 170 to 300 K [4]. In the monocrystal, neither polygonalisation of zirconia nor amorphisation was found for ion doses below 1×10^{15} cm^{-2}, corresponding to 4 dpa. Damage accumulation in Xe-ion irradiated stabilised zirconia was found to progress in three stages: (i) formation of defect clusters, (ii) transition stage in which damage increases rapidly over a small range of ion dose, due to the linking of dislocations and defect clusters, (iii) saturation stage in which damage accumulation is retarded or increases only slowly with ion dose. The composition of stabilised zirconia does not seem to influence the dose dependence of these damage stages.

Combining the experiments at low Xe ion energy (60 keV) from 300 up to 925 K and with more energetic Xe ions (1.5 MeV) down to 20 K, Degueldre et al. [8] demonstrated that on polycrystalline samples amorphisation does not occur up to doses of 2×10^{16} cm^{-2}. During the low energy tests, Xe bubbles were formed. These implantations concern only sub-microscopic thick samples and not of bulk pellets.

Recently, Garrido et al. [22] compared the effect of low doses (10^{14} cm^{-2}) of 340 MeV xenon ion irradiation on stabilised cubic zirconia and uranium dioxide. For this heavy ion energy, ionisation mechanisms prevail. Only polygonalisation was observed but no amorphisation.

All this work demonstrates clearly that stabilised zirconia is not amorphised during Xe ion irradiation, whatever the fluence (not exceeding 1×10^{15} cm^{-2}), the stabilising element and the temperature of the sample. However, the potential diffusion of xenon in the bulk of the material has not yet been addressed.

In this study, the behaviour of xenon in macroscopic samples of YSZ is investigated theoretically as a function of energy and composition of the IMF material, and experimentally for its retention after xenon ion implantation into polycrystalline $Y_{0.15}Zr_{0.85}O_{1.925}$ samples. The implantation depth was selected in order to subsequently apply the Rutherford backscattering spectrometry (RBS) to determine the xenon distribution. The effect of temperature on the potential diffusion of the xenon was measured after annealing the sample at progressively increasing temperatures and by repeating the RBS analysis. Comparison of diffusion properties of Xe with Cs and I as dopants, and the comparison of Xe diffusion in UO_2 were carried out as a function of temperature. The retention behaviour of xenon was analysed in a comprehensive way, taking into account the size of the considered species in the YSZ lattice.

2. Theoretical background

The simulation code the stopping and ranges of ions in matter (SRIM)-2000 [23] was used to calculate the penetration depth of Xe as a function of ion energy, inert matrix composition and implantation profiles (i.e., Xe concentration C as a function of depth x in the sample). The implantation of 600 keV Xe^{3+} ions was simulated to estimate the RBS spectrum expected experimentally. For this incident ion energy, the implantation profile followed precisely a double Gaussian distribution that could be simplified as a single Gaussian in first approximation.

The dopant distribution enlarges with time t (after implantation) according to the equation [9,10]:

$$C(x,t) = \frac{\Phi}{2\sqrt{\pi(D \cdot t + \sigma_0^2/2)}} \exp\left(-\frac{(x - x_0)^2}{4 \cdot D \cdot t + 2 \cdot \sigma_0^2} \right), \tag{1}$$

where σ_0 (nm) is the initial variance, Φ (cm^{-2}) the ion fluence, x_0 (nm) the average implantation depth of the Gaussian distribution in the sample, t (s) the time of diffusion after initiation and D (cm^2 s^{-1}) is the diffusion coefficient. Diffusion enlarges the double Gaussian distribution. Their variances are consequently a function of time and temperature. For a given temperature (i.e., D constant), the behaviour of the variance is given by

$$\sigma(t) = \sqrt{2 \cdot D \cdot t + \sigma_0^2}. \tag{2}$$

The diffusion coefficient may be extracted from Eq. (2). However, during the thermal treatment no modification of the distribution is observed. A maximum

value of the diffusion coefficient may be estimated using the error derivation:

$$\Delta D = \frac{\Delta\sigma_0^2}{t}, \tag{3}$$

where ΔD is the error on the diffusion coefficient (in this case its detection limit or its maximum value), $\Delta\sigma$ the error on the variance of the profile, assuming that the error on the time is negligible and $\Delta\sigma \approx \Delta\sigma_0$.

3. Experimental

The samples used in the implantation tests were YSZ pellets. The starting materials were the oxide powder ZrO_2 (hafnium free <0.1 at.%) and Y_2O_3. These powders were mixed together to result in a product with 15 at.%Y for the Zr–Y ratio and milled in a milling machine of the type 'Retsch Fliehkraftmuehle'. A dry milling procedure of 2 h was performed, and the powders were homogenised in a tubular mixer. The milling procedure was repeated, and the resulting powder was pressed to pellets using the press Meyer CAUO-10PCM30 with a 8 and 10 mm punch, the pressure being 320 and 360 MPa, respectively. The sintering was performed in a Heraeus NiCr–Ni oven with a heating rate of 5 K min^{-1} to 1073 K for 2 h in the first step and then to 1873 K for 10 h in the second step. Unforced cooling followed. The resulting $Y_{0.15}Zr_{0.85}O_{1.925}$ pellets of 7.0 and 8.9 mm diameter had a relative density of about 90% for a theoretical density of 5.89 g cm^{-3} determined from lattice parameter measurements. Pellets were cut in 1 mm slices to set the disc samples on the holder of the implantation unit.

Dopant implantations were both performed at the Ion Beam Material Science Laboratory of Los Alamos National Laboratory with the 200 kV Varian CF-3000 ion implanter [24]. The implantation was carried out with a beam of 200 nA of 540 keV Xe^{3+} ions. The implantation fluences were $\Phi = 0.4 \times 10^{15}$ and 4×10^{15} cm^{-2} on 0.62 cm^2 area. The ions were implanted under normal incidence at room temperature.

The RBS analyses were performed with the PSI/ETH Tandem accelerator [25]. The resulting xenon depth profiles were measured by 5 MeV ^4He RBS performed under standard conditions [26]. After implantation and a first RBS analysis, the sample was heat treated at different temperatures. RBS analysis (at room temperature) was performed after each thermal treatment. The thermal treatments were performed at 873 K and by successive steps of 100 K up to 1773 K for 2 h with a heating rate of 10 K min^{-1} using the Hereaus NiCr–Ni oven. All thermal treatments were performed on the same sample. Consequently, previous annealing cycles have to be taken into account for a correct interpretation of the results.

TEM has been carried out at Ecole Polytechnique Fédérale de Lausanne (EPFL) on a Phillips CM300 FEG (operating at 300 kV with a field emission gun) equipped with a gatan imaging filter (GIF) and an EDX detector. The GIF imaging filter allows to perform electron spectroscopic imaging (ESI), as well as electron energy loss spectroscopy (EELS), on the material. Each specimen was prepared according to the tripod technique on a transverse section. The final stage of specimen preparation was carried out by ion beam milling in order to avoid the destruction of the specimen near the implanted edge.

4. Results and discussion

4.1. Dopant implantation penetration depth

Calculation of the penetration depth of xenon in the zirconia-based IMF: $Er_{\xi Er}Y_{\xi Y}An_{\xi An}Zr_{1-(\xi Er+\xi Y+\xi An)}O_{2-(\xi Er+\xi Y)/2}$ (with An = U or Pu), was performed as a function of Xe ion energy and the composition of the IMF. Results of these calculations are given in Fig. 1.

The energy dependence of the xenon ion penetration depth in zirconia shows three parts in the plot (Fig. 1(a)): the first from 10 to 100 keV corresponds to nuclear stopping, the third above 1 MeV is due to electronic stopping interaction, and in between, from 100 keV to 1 MeV, nuclear stopping decreases and electronic interactions are not yet predominant. In this latter range, the penetration of xenon is more efficient and the slope on the plot increases. Since zirconium and yttrium have similar atomic numbers and masses and erbium is only present at the 5 metal–atom% level, the effect of the composition was studied on the simplified system: $An_{\xi An}Zr_{1-\xi An}O_2$ with ξ An the atomic fraction of the actinide An (with An = U or Pu). The result shown in Fig. 1(b) indicates that in the zirconia IMF, the fission product mean penetration depth will be of the order of 5–10 μm and that the dopant (a few % only) concentration in zirconia has a small effect on the penetration depth. Consequently, a composite material Zr– or $MgAl_2O_4$–$Er_{0.05}Y_{0.10}Pu_{0.10}$ $Zr_{0.75}O_{1.925}$ will be optimal for micro-spheres of zirconia-doped material of the order of 200 μm size i.e., about 20 times the stopping range of xenon in zirconia. This result is a compromise between the fissile material carrier and the surrounding inert matrix. Zirconia whose thermal conductivity is rather low requires small spheres for heat transfer, but the radiation transfer of fission products from the doped zirconia phase into the more fragile surrounding material of the composite fuel requires large spheres for optimal retention.

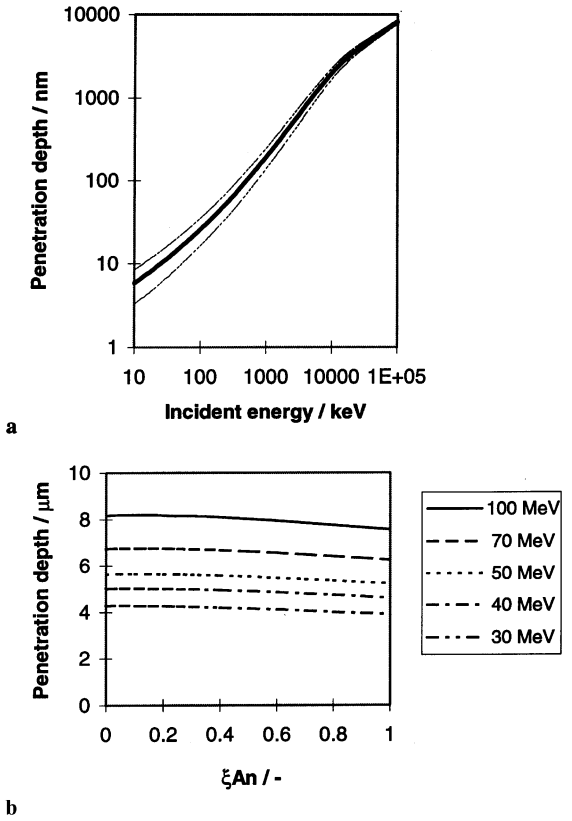

Fig. 1. Penetration depth of Xe in doped or undoped YSZ as calculated by SRIM. (a) Effect of the Xe ion energy on the average penetration depth in ZrO_2 or $Y_{0.15}Zr_{0.85}O_{1.925}$. (b) Effect of the actinide concentration on the penetration depth of Xe ions in $An_{\xi An}Zr_{1-\xi An}O_2$, with An = U for Pu.

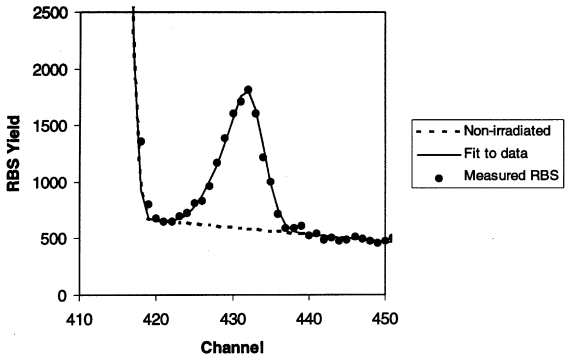

Fig. 2. RBS spectrum of YSZ implanted with 4×10^{15} Xe ion/cm^2. Dashed line: simulated spectrum for unimplanted sample; Solid line: simulated spectrum for implanted sample; Dots: measured spectrum of sample annealed at 1273 K for 2 h.

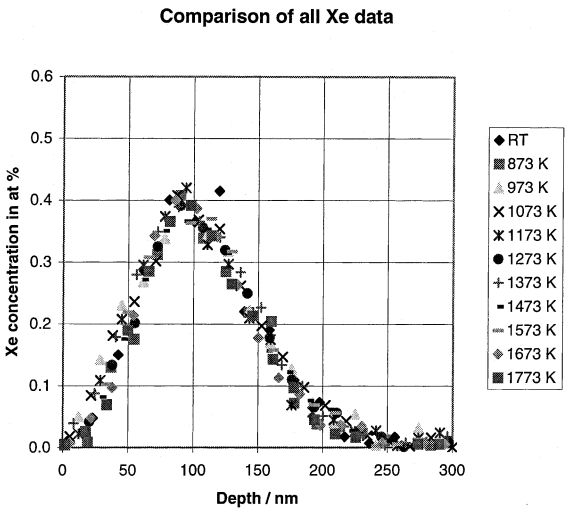

Fig. 3. Xe profiles deduced from RBS spectra after each annealing step. Conditions: at room temperature and after 2 h at each temperature step, Xe fluence: 4×10^{15} cm^{-2}. Note, the height of the peak is not affected by the thermal treatment.

4.2. RBS analysis before and after thermal treatment

Fig. 2 shows an example of RBS raw data for the sample annealed at 1273 K for 2 h. The simulated spectrum that reproduces the experimental data was calculated using the code RUMP [27].

For xenon implantation in YSZ, the detailed depth profile calculated by SRIM can perfectly be represented by a double Gaussian, however, it can be well approximated by a single one. For each temperature step, the RBS spectrum was therefore fitted by a Gaussian profile. The mean depth of the Gaussian x_0 and the fluence Φ were kept constant, the only fitting parameter was the variance σ.

From the measured RBS raw data shown in Fig. 2, the depth profile was extracted by substracting the background of the non-implanted matrix and converting the RBS energy scale into a depth scale. Fig. 3 shows a compilation of the resulting profiles at all temperatures. It was striking to find no significant release of xenon up to 1773 K. After annealing at 1773 K, no significant enlargement of the xenon distribution and no decrease in the distribution height were observed, indicating full xenon retention in the sample. Thus, xenon's apparent diffusion was not measurable even at a temperature of 1773 K. From the fitted variances after the thermal treatments, the limit of D was calculated using Eq. (3). The estimated error on the variance is 5 nm, corresponding to a ΔD of 3×10^{-21} m^{-2} s^{-1} on the diffusion coefficient (given by Eq. (3)). The maximal diffusion coefficient is then ΔD of 3×10^{-21} m^{-2} s^{-1}.

4.3. TEM analysis

The transverse specimen prepared for the TEM analysis was studied in order to obtain information

about the spatial distribution of xenon in the YSZ matrix. Owing to the very low concentration of the Xe in the matrix, a direct observation of the Xe clusters was not possible in the bright field images. The imaging filter was therefore used to observe the trace of the material in the matrix using the plasmon peaks [28,29]. Fig. 4 presents a typical TEM plasmon image. At a depth of 100 ± 80 nm a population of 6 nm large bubbles is observed. The distribution is however larger than that calculated by SRIM. It agrees however well with that measured by RBS.

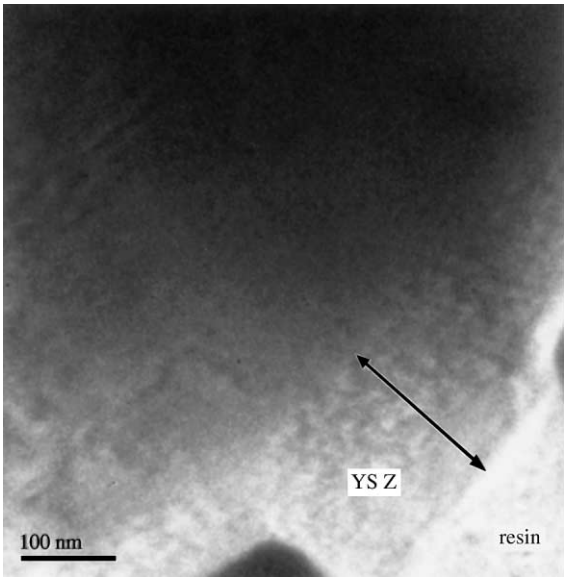

Fig. 4. Xe distribution determined by TEM before annealing. Conditions: YSZ sample implanted with Xe ion fluence of 4×10^{14} cm^{-2}. Note: resin in white on right side, the arrow: 180 nm showing the bubble-rich area (please refer to text for details).

4.4. Interpretation of the retention mechanism

To understand the reason for the excellent retention of Xe by zirconia, mechanisms of implantation and molecular embedding of xenon must be revisited. After Xe implantation, zirconia along the ion pathway does not undergo amorphisation but re-crystallises in cubic solid solution as verified earlier [8]. In the cubic solid solution, xenon remains atomic and due to its large size it does not find its place in the cation or anion sub-lattice (see Table 1). Consequently, segregation occurs leading to the formation of nanobubbles. The presence of bubbles may be suggested for large doses [8], while dissolution of elemental Xe may also be postulated for very low Xe doses. For the doses investigated here, a small fraction of Xe may be soluble after implantation, the rest of which may generate bubbles, as described earlier [8].

After xenon implantation, the atoms are distributed in the bulk of grains, whose sizes are of the order of 2000 μm. The design of the experiment fulfils the following inequation:

$$\text{Grain size } (2000 \text{ nm}) > x_0\ (100 \text{ nm}) > \sigma = \sigma_0(50 \text{ nm}).$$

Table 1 summarises the relevant parameters to discuss the retention properties of the species compared to the auto-diffusion process of the main components of the inert matrix. Clearly, if Xe is trapped, its potential migration in the cation sub-lattice is sterically impossible because of the size difference between Xe (220 pm) and Zr^{4+} (84 pm). If Xe finds its initial hosting place in the anion sub-lattice again, its size is larger than the oxygen ions (140 pm) or vacancies (160 pm) making movement extremely difficult.

Comparison between the behaviour of Xe in UO_2 and ZrO_2, and of I, Xe and Cs in ZrO_2 is very interesting. It is impossible to apply the implantation and RBS analysis to characterise the diffusion properties of Xe in UO_2. Implantation is possible but the RBS analysis is very difficult because the Xe peak appears above

Table 1
Comparison of important parameters to account for diffusion mechanism interpretation[a]

Species	D (m^2 s^{-1})	Ref.		r_{max}(pm)		r_{min}(pm)	Ref.
Xe	$<1.3 \times 10^{-20}$	This work	Xe^0	220	Xe^0	220	[30]
I	4×10^{-19}	[31]	I^-	220	I^0	198[b]	[34,35]
Cs	5×10^{-17}	[31]	Cs^0	298[c]	Cs^+	174	[34,35]
O^{2-}	3×10^{-9}–10^{-10}	[32,33]	CN 6	140	CN 3	136	[35]
Ov	–	–		172		160	[36]
Zr^{4+}	3×10^{-20}	[33]	CN 8	84	CN 6	72	[35]
Y^{3+}	–	–	CN 8	109	CN 6	90	[35]
U^{4+}	3×10^{-22}	[33]	CN 8	95		–	[37]

[a] Conditions: D at 1500 K, CN coordination number.
[b] van der Waals.
[c] Covalent.

the U edge preventing sensitive analysis. The only data are provided by the release of fission products (e.g., Xe) from lightly irradiated polycrystalline UO_2 samples [28]. Comparison of the Xe diffusion coefficient values in UO_2 and ZrO_2 is given in Fig. 5(a). The lines A–E show the variability of the data for the different samples and under various irradiation conditions. Xe diffuses faster in UO_2 than in ZrO_2. It is assumed that this is due to a larger solubility of Xe in UO_2 (larger lattice parameter size and larger polarisability) than in ZrO_2.

In addition, the diffusion coefficients of Xe, I and Cs, as reported in [31], are compared in Fig. 5(b). The following is found: $D_{Cs} > D_I > D_{Xe}$. These inequations follow the trend of the solubility of these species in the zirconia cubic solution. This is also due to the radii of Cs^+ and I^0 (species identified after implantation [9,10]) that are smaller than Xe (Table 1). One could also note that the reason for Xe immobility is its inertness in ZrO_2 inert matrix.

Since the Xe apparent diffusion coefficient was found to be below the experimental detection limit, it may be concluded that the only xenon movement in the matrix would be provided by the diffusion of the bubbles themselves. This would begin at higher temperatures [38] for which the partial pressure of ZrO_2 also increases allowing bubble migration in the inert matrix.

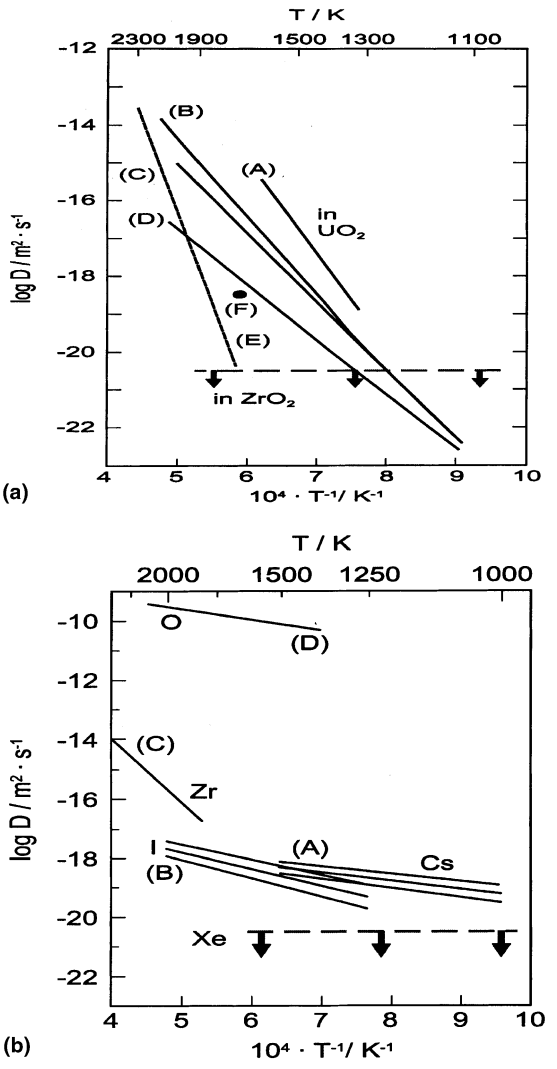

Fig. 5. Comparison of diffusion coefficient. (a) Xe in stabilised ZrO_2 and in UO_2, data from [37]; (b) Xe with Cs and I in stabilised ZrO_2, data from [31].

5. Conclusion

Progress has been made to understand the retention behaviour of Xe in zirconia-based IMF material. Strong retention of implanted xenon in YSZ is observed up to 1773 K. Because of its inertness, Xe is likely to be insoluble in zirconia and forms nanobubbles at high temperature. The migration of these features is very slow, which also contributes to the attractiveness of the zirconia inert matrix as an advanced nuclear fuel.

Acknowledgements

The authors thank Drs F. Ingold, M. Burghartz and Ch. Hellwich for the stimulating discussions. P. Heimgartner participated in the preparation of the samples. TEM analysis was performed at Ecole Polytechnique Fédérale de Lausanne (EPFL).

References

[1] C. Degueldre, U. Kasemeyer, F. Botta, G. Ledergerber, Mater. Res. Soc. Symp. Proc. 412 (1996) 15.
[2] C. Degueldre, J.M. Paratte, Nucl. Technol. 123 (1998) 21.
[3] F. Vettraino, G. Magnani, T. LaTorretta, E. Marmo, S. Coelli, L. Luzzi, P. Ossi, G. Zappa, J. Nucl. Mater. 274 (1999) 23.
[4] K. Sickafus, H. Matzke, T. Hartmann, K. Yasuda, J. Valdez, P. Chodak III, M. Nastasi, R. Verrall, J. Nucl. Mater. 274 (1999) 66.
[5] R. Konings, K. Bakker, J. Boshoven, H. Hein, M. Huntelaar, R. van der Laan, J. Nucl. Mater. 274 (1999) 84.
[6] T. Yamashita, N. Nitani, H. Kanazawa, M. Magara, T. Ohmihi, H. Takano, T. Muromura, J. Nucl. Mater. 274 (1999) 98.
[7] C. Degueldre, J.M. Paratte, J. Nucl. Mater. 274 (1999) 1.
[8] C. Degueldre, P. Heimgartner, G. Ledergerber, N. Sasajima, K. Hojou, T. Muromura, L. Wang, W. Gong, R. Ewing, Mater. Res. Soc. Symp. Proc. 439 (1997) 625.

[9] M.A. Pouchon, M. Doebeli, C. Degueldre, Nucl. Instrum. and Meth. B 148 (1999) 783.
[10] M.A. Pouchon, M. Doebeli, C. Degueldre, M. Burghartz, J. Nucl. Mater. 274 (1999) 61.
[11] M. Paraschiv, A. Paraschiv, V. Grecu, J. Nucl. Mater. 275 (1999) 164.
[12] M. Norton, W. Jiang, P. Kotula, Scripta Metallurg. Materialia 31 (1994) 555.
[13] T. Levine, J. Keddie, P. Revesz, J. Mayer, E. Giannelis, J. Am. Ceram. Soc. 76 (1993) 1369.
[14] T. Levine, E. Giannelis, P. Kodali, J. Tesmer, M. Nastasi, J. Mayer, Proc. Mater. Res. Soc. November 1993 (1994) 6.
[15] E. Fleischer, M. Norton, M. Zaleski, W. Hertl, C. Carter, J. Mayer, J. Mater. Res. 6 (1991) 1905.
[16] M. Norton, W. Jiang, J. Dickinson, L. Jensen, S. Langford, E. Fleischer, J. Mayer, J. Am. Ceram. Soc. 76 (1993) 2076.
[17] N. Sasajima, T. Matsui, K. Hojou, S. Furuno, H. Otsu, K. Izui, T. Muromura, Nucl. Instrum. and Meth. B 141 (1998) 487.
[18] N. Yu, K. Sikafus, P. Kodali, M. Nastasi, J. Nucl. Mater. 244 (1997) 266.
[19] N. Yu, T. Levine, K. Sikafus, M. Nastasi, J. Michell, C. Maggiore, C. Evans, M. Hollander, J. Tesmer, W. Weber, J. Mayer, Nucl. Instrum. and Meth. B 141 (1996) 358.
[20] K. Sickafus, C. Wettland, N. Baker, N. Yu, R. Devanathan, M. Nastasi, N. Bordes, Mater. Sci. Eng. 253 (1998) 78.
[21] K. Yasuda, M. Nastasi, K. Sickafus, C. Maggiore, Nucl. Instrum. and Meth. B 136–138 (1998) 499.
[22] L. Thomé, A. Garido, J. Jagielski, J. Nucl. Mater. (to be published).
[23] SRIM: http://www.research.ibm.com/ionbeams/SRIM/SRIM LEGL.HTiegler@watson.ibm.com iegler@watson. ibm.com.
[24] http://www.lanl.gov/orgs/cipto/DTIN/open/UsrFac/userfac25.html.
[25] Accelerator: http://www.phys.ethz.ch/IPP/tandem/Welcome.html.
[26] W.K. Chu, J.W. Mayer, M.A. Nicolet, Backscattering Spectrometry, Academic Press, New York, 1978.
[27] L.R. Doolitle, Nucl. Instrum. and Meth. B 15 (1986) 227.
[28] L. Reimer, in: P.W. Hawkes (Ed.), Energy Filtering Transmission Electron Microscopy. Springer Series in Optical Sciences, vol. 71, Springer, Berlin.
[29] S. Abolhassani Dadras, G. Vazquez Nin, O. Echeverria, S. Fakan, J. Microscopy. 183 (3) (1996) 215.
[30] http:/www.webelement.com /webelements/element.
[31] C. Degueldre, M. Pouchon, M. Doebeli, G. Ledergerber, Mater. Res. Soc. Symp. 540 (1999) 337.
[32] C. Perry, A. Feinberg, Solid State Commun. 36 (1980) 519.
[33] Y. Sakka, Y. Oishi, K. Ando, S. Morita, J. Am. Ceram. Soc. 74 (1991) 2610.
[34] Periodic Table (key data). http:/www.shef.ac.uk/chemistry/web-element/fr-key/.
[35] R. Shannon, M. Prewitt, Acta Cryst. B25 (1969) 925.
[36] C. Degueldre, M. Takano, T. Ohmishi, K. Fukuda, P. Heimgartner, T. JAERI research 97-087, Tokai-Mura, Ibaraki-ken, Japan.
[37] S. Prussin, D. Olander, W. Lau, L. Hansson, J. Nucl. Mater. 154 (1988) 25.
[38] J. Fleig, J. Maier, J. Am. Ceram. Soc. 82 (1999) 3485.